MarioNETte: Few-shot Face Reenactment Preserving Identity of Unseen Targets

Sungjoo Ha*, **Martin Kersner***, **Beomsu Kim***, **Seokjun Seo***, **Dongyoung Kim**[†]

Hyperconnect
Seoul, Republic of Korea
{shurain, martin.kersner, beomsu.kim, seokjun.seo, dongyoung.kim}@hpcnt.com

Abstract

When there is a mismatch between the target identity and the driver identity, face reenactment suffers severe degradation in the quality of the result, especially in a few-shot setting. The identity preservation problem, where the model loses the detailed information of the target leading to a defective output, is the most common failure mode. The problem has several potential sources such as the identity of the driver leaking due to the identity mismatch, or dealing with unseen large poses. To overcome such problems, we introduce components that address the mentioned problem: image attention block, target feature alignment, and landmark transformer. Through attending and warping the relevant features, the proposed architecture, called MarioNETte, produces high-quality reenactments of unseen identities in a few-shot setting. In addition, the landmark transformer dramatically alleviates the identity preservation problem by isolating the expression geometry through landmark disentanglement. Comprehensive experiments are performed to verify that the proposed framework can generate highly realistic faces, outperforming all other baselines, even under a significant mismatch of facial characteristics between the target and the driver.

Introduction

Given a *target* face and a *driver* face, face reenactment aims to synthesize a *reenacted* face which is animated by the movement of a driver while preserving the identity of the target.

Many approaches make use of generative adversarial networks (GAN) which have demonstrated a great success in image generation tasks. Xu et al.; Wu et al. (2017; 2018) achieved high-fidelity face reenactment results by exploiting CycleGAN (Zhu et al. 2017). However, the CycleGAN-based approaches require at least a few minutes of training data for each target and can only reenact predefined identities, which is less attractive in-the-wild where a reenactment of unseen targets cannot be avoided.

The few-shot face reenactment approaches, therefore, try to reenact any unseen targets by utilizing operations such

Figure 1: Examples of identity preservation failures and improved results generated by the proposed method. Each row shows (a) driver shape interference, (b) losing details of target identity, and (c) failure of warping at large poses.

as adaptive instance normalization (AdaIN) (Zakharov et al. 2019) or warping module (Wiles, Koepke, and Zisserman 2018; Siarohin et al. 2019). However, current state-of-the-art methods suffer from the problem we call *identity preservation problem*: the inability to preserve the identity of the target leading to defective reenactments. As the identity of the driver diverges from that of the target, the problem is exacerbated even further.

Examples of flawed and successful face reenactments, generated by previous approaches and the proposed model, respectively, are illustrated in Figure 1. The failures of previous approaches, for the most part, can be broken down into three different modes [1]:

1. Neglecting the identity mismatch may lead to a identity of the driver interfere with the face synthesis such that the generated face resembles the driver (Figure 1a).

---

*Equal contributions, listed in alphabetical order.

[†]Corresponding author.

---

[1]Additional example images and videos can be found at the following URL: http://hyperconnect.github.io/MarioNETte
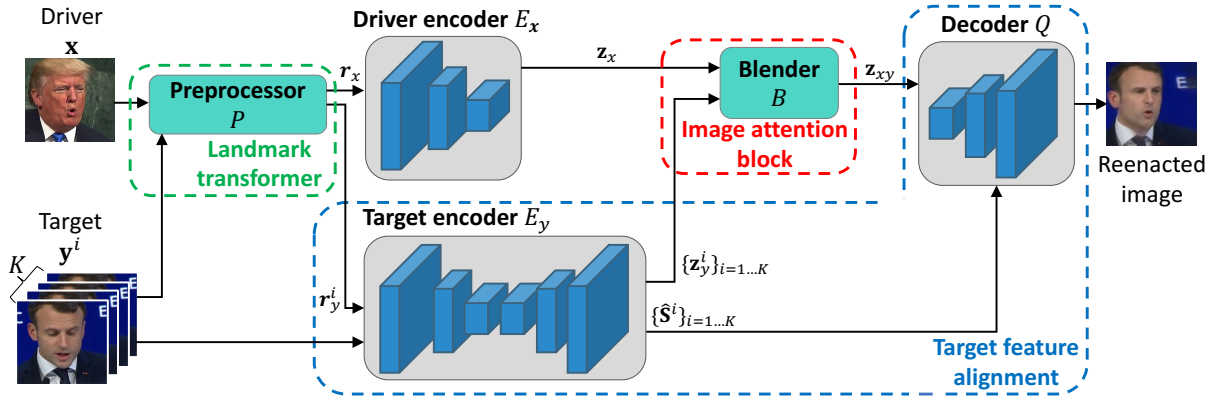
Figure 2: The overall architecture of MarioNETte.

2. Insufficient capacity of the compressed vector representation (e.g., AdaIN layer) to preserve the information of the target identity may lead the produced face to lose the detailed characteristics (Figure 1b).

3. Warping operation incurs a defect when dealing with large poses (Figure 1c).

We propose a framework called *MarioNETte*, which aims to reenact the face of unseen targets in a few-shot manner while preserving the identity without any fine-tuning. We adopt *image attention block* and *target feature alignment*, which allow MarioNETte to directly inject features from the target when generating image. In addition, we propose a novel *landmark transformer* which further mitigates the identity preservation problem by adjusting for the identity mismatch in an unsupervised fashion. Our contributions are as follows:

- We propose a few-shot face reenactment framework called MarioNETte, which preserves the target identity even in situations where the facial characteristics of the driver differs widely from those of the target. Utilizing image attention block, which allows the model to attend to relevant positions of the target feature map, together with target feature alignment, which includes multiple feature-level warping operations, proposed method improves the quality of the face reenactment under different identities.

- We introduce a novel method of landmark transformation which copes with varying facial characteristics of different people. The proposed method adapts the landmark of a driver to that of the target in an unsupervised manner, thereby mitigating the identity preservation problem without any additional labeled data.

- We compare the state-of-the-art methods when the target and the driver identities coincide and differ using VoxCeleb1 (Nagrani, Chung, and Zisserman 2017) and CelebV (Wu et al. 2018) dataset, respectively. Our experiments including user studies show that the proposed method outperforms the state-of-the-art methods.

MarioNETte Architecture

Figure 2 illustrates the overall architecture of the proposed model. A conditional *generator* G generates the reenacted face given the driver $\mathbf{x}$ and the target images $\{\mathbf{y}^i\}_{i=1...K}$, and the *discriminator* D predicts whether the image is real or not. The generator consists of following components:

- The **preprocessor** P utilizes a 3D landmark detector (Bulat and Tzimiropoulos 2017) to extract facial keypoints and renders them to landmark image, yielding $\mathbf{r}_x = P(\mathbf{x})$ and $\mathbf{r}_y^i = P(\mathbf{y}^i)$, corresponding to the driver and the target input respectively. Note that proposed landmark transformer is included in the preprocessor. Since we normalize the scale, translation and rotation of landmarks before using them in a landmark transformer, we utilize 3D landmarks instead of 2D ones.

- The **driver encoder** $E_x(\mathbf{r}_x)$ extracts pose and expression information from the driver input and produces driver feature map $\mathbf{z}_x$.

- The **target encoder** $E_y(\mathbf{y}, \mathbf{r}_y)$ adopts a U-Net architecture to extract style information from the target input and generates target feature map $\mathbf{z}_y$ along with the warped target feature maps $\hat{\mathbf{S}}$.

- The **blender** $B(\mathbf{z}_x, \{\mathbf{z}_y^i\}_{i=1...K})$ receives driver feature map $\mathbf{z}_x$ and target feature maps $\mathbf{Z}_y = [\mathbf{z}_y^1, \ldots, \mathbf{z}_y^K]$ to produce mixed feature map $\mathbf{z}_{xy}$. Proposed image attention block is basic building block of the blender.

- The **decoder** $Q(\mathbf{z}_{xy}, \{\hat{\mathbf{S}}^i\}_{i=1...K})$ utilizes warped target feature maps $\hat{\mathbf{S}}$ and mixed feature map $\mathbf{z}_{xy}$ to synthesize reenacted image. The decoder improves quality of reenacted image exploiting proposed target feature alignment.

For further details, refer to Supplementary Material A1.

Image attention block

To transfer style information of targets to the driver, previous studies encoded target information as a vector and mixed it with driver feature by concatenation or AdaIN layers (Liu et al. 2019; Zakharov et al. 2019). However, encoding targets
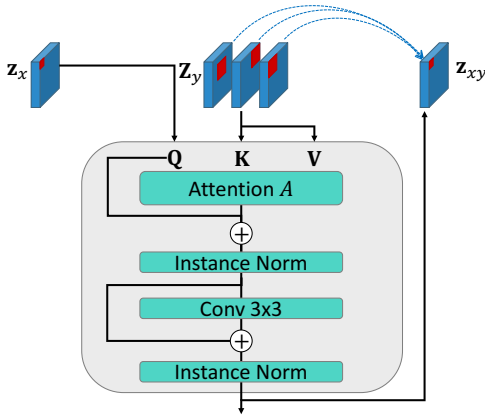
Figure 3: Architecture of the image attention block. Red boxes conceptually visualize how each position of $\mathbf{z}_x$ and $\mathbf{Z}_y$ are associated. Our attention can attend different position of each target feature maps with different importance.

Figure 4: Architecture of target feature alignment.

as a spatial-agnostic vector leads to losing spatial information of targets. In addition, these methods are absent of innate design for multiple target images, and thus, summary statistics (e.g. mean or max) are used to deal with multiple targets which might cause losing details of the target.

We suggest image attention block (Figure 3) to alleviate aforementioned problem. The proposed attention block is inspired by the encoder-decoder attention of transformer (Vaswani et al. 2017), where the driver feature map acts as an attention query and the target feature maps act as attention memory. The proposed attention block attends to proper positions of each feature (red boxes in Figure 3) while handling multiple target feature maps (i.e., $\mathbf{Z}_y$).

Given driver feature map $\mathbf{z}_x \in \mathbb{R}^{h_x \times w_x \times c_x}$ and target feature maps $\mathbf{Z}_y = [\mathbf{z}_y^1, \ldots, \mathbf{z}_y^K] \in \mathbb{R}^{K \times h_y \times w_y \times c_y}$, the attention is calculated as follows:

$$
\begin{aligned}
\mathbf{Q} &= \mathbf{z}_x \mathbf{W}_q + \mathbf{P}_x \mathbf{W}_{qp} &&\in \mathbb{R}^{h_x \times w_x \times c_a} \\
\mathbf{K} &= \mathbf{Z}_y \mathbf{W}_k + \mathbf{P}_y \mathbf{W}_{kp} &&\in \mathbb{R}^{K \times h_y \times w_y \times c_a} \quad (1) \\
\mathbf{V} &= \mathbf{Z}_y \mathbf{W}_v &&\in \mathbb{R}^{K \times h_y \times w_y \times c_x}
\end{aligned}
$$

$$
A(\mathbf{Q}, \mathbf{K}, \mathbf{V}) = \mathrm{softmax}\left(\frac{f(\mathbf{Q})f(\mathbf{K})^T}{\sqrt{c_a}}\right) f(\mathbf{V}), \quad (2)
$$

where $f : \mathbb{R}^{d_1 \times \ldots \times d_k \times c} \to \mathbb{R}^{(d_1 \times \ldots \times d_k) \times c}$ is a flattening function, all $\mathbf{W}$ are linear projection matrices that map to proper number of channels at the last dimension, and $\mathbf{P}_x$ and $\mathbf{P}_y$ are sinusoidal positional encodings which encode the coordinate of feature maps (further details of sinusoidal positional encodings we used are described in Supplementary Material A2). Finally, the output $A(\mathbf{Q}, \mathbf{K}, \mathbf{V}) \in \mathbb{R}^{(h_x \times w_x) \times c_x}$ is reshaped to $\mathbb{R}^{h_x \times w_x \times c_x}$.

Instance normalization, residual connection, and convolution layer follow the attention layer to generate output feature map $\mathbf{z}_{xy}$. The image attention block offers a direct mechanism of transferring information from multiple target images to the pose of driver.
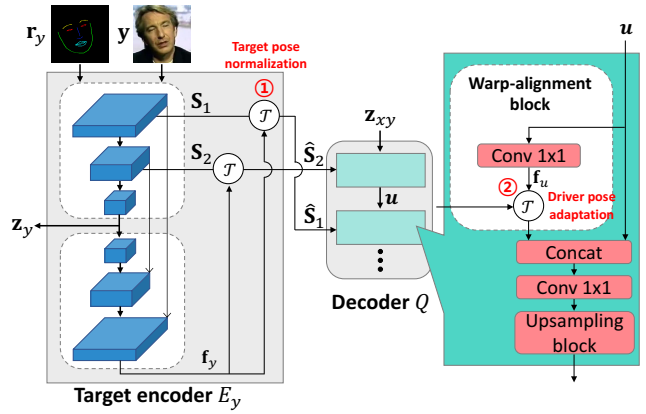
Target feature alignment

The fine-grained details of the target identity can be preserved through the warping of low-level features (Siarohin et al. 2019). Unlike previous approaches that estimate a warping flow map or an affine transform matrix by computing the difference between keypoints of the target and the driver (Balakrishnan et al. 2018; Siarohin et al. 2018; Siarohin et al. 2019), we propose a target feature alignment (Figure 4) which warps the target feature maps in two stages: (1) *target pose normalization* generates pose normalized target feature maps and (2) *driver pose adaptation* aligns normalized target feature maps to the pose of the driver. The two-stage process allows the model to better handle the structural disparities of different identities. The details are as follows:

1. **Target pose normalization.** In the target encoder E_y, encoded feature maps $\{\mathbf{S}_j\}_{j=1\ldots n_y}$ are processed into $\hat{\mathbf{S}} = \{\mathcal{T}(\mathbf{S}_1; \mathbf{f}_y), \ldots, \mathcal{T}(\mathbf{S}_{n_y}; \mathbf{f}_y)\}$ by estimated normalization flow map $\mathbf{f}_y$ of target and warping function $\mathcal{T}$ (① in Figure 4). The following *warp-alignment block* at decoder treats $\hat{\mathbf{S}}$ in a target pose-agnostic manner.

2. **Driver pose adaptation.** The warp-alignment block in the decoder receives $\{\hat{\mathbf{S}}^i\}_{i=1\ldots K}$ and the output $\mathbf{u}$ of the previous block of the decoder. In a few-shot setting, we average resolution-compatible feature maps from different target images (i.e., $\hat{\mathbf{S}}_j = \sum_i \hat{\mathbf{S}}_j^i / K$). To adapt pose-normalized feature maps to the pose of the driver, we generate an estimated flow map of the driver $\mathbf{f}_u$ using 1×1 convolution that takes $\mathbf{u}$ as the input. Alignment by $\mathcal{T}(\hat{\mathbf{S}}_j; \mathbf{f}_u)$ follows (② in Figure 4). Then, the result is concatenated to $\mathbf{u}$ and fed into the following residual upsampling block.

Landmark Transformer

Large structural differences between two facial landmarks may lead to severe degradation of the quality of the reenactment. The usual approach to such a problem has been to learn a transformation for every identity (Wu et al. 2018) or

by preparing a paired landmark data with the same expressions (Zhang et al. 2019). However, these methods are unnatural in a few-shot setting where we handle unseen identities, and moreover, the labeled data is hard to be acquired. To overcome this difficulty, we propose a novel *landmark transformer* which transfers the facial expression of the driver to an arbitrary target identity. The landmark transformer utilizes multiple videos of unlabeled human faces and is trained in an unsupervised manner.

Landmark decomposition

Given video footages of different identities, we denote $\mathbf{x}(c, t)$ as the t-th frame of the c-th video, and $\mathbf{l}(c, t)$ as a 3D facial landmark. We first transform every landmark into a normalized landmark $\bar{\mathbf{l}}(c, t)$ by normalizing the scale, translation, and rotation. Inspired by 3D morphable models of face (Blanz and Vetter 1999), we assume that normalized landmarks can be decomposed as follows:

$$\bar{\mathbf{l}}(c, t) = \bar{\mathbf{l}}_m + \bar{\mathbf{l}}_{id}(c) + \bar{\mathbf{l}}_{exp}(c, t), \tag{3}$$

where $\bar{\mathbf{l}}_m$ is the average facial landmark geometry computed by taking the mean over all landmarks, $\bar{\mathbf{l}}_{id}(c)$ denotes the landmark geometry of identity c, computed by $\bar{\mathbf{l}}_{id}(c) = \sum_t \bar{\mathbf{l}}(c, t)/T_c - \bar{\mathbf{l}}_m$ where T_c is the number of frames of c-th video, and $\bar{\mathbf{l}}_{exp}(c, t)$ corresponds to the expression geometry of t-th frame. The decomposition leads to $\bar{\mathbf{l}}_{exp}(c, t) = \bar{\mathbf{l}}(c, t) - \bar{\mathbf{l}}_m - \bar{\mathbf{l}}_{id}(c)$.

Given a target landmark $\bar{\mathbf{l}}(c_y, t_y)$ and a driver landmark $\bar{\mathbf{l}}(c_x, t_x)$ we wish to generate the following landmark:

$$\bar{\mathbf{l}}(c_x \rightarrow c_y, t_x) = \bar{\mathbf{l}}_m + \bar{\mathbf{l}}_{id}(c_y) + \bar{\mathbf{l}}_{exp}(c_x, t_x), \tag{4}$$

i.e., a landmark with the identity of the target and the expression of the driver. Computing $\bar{\mathbf{l}}_{id}(c_y)$ and $\bar{\mathbf{l}}_{exp}$ is possible if enough images of c_y are given, but in a few-shot setting, it is difficult to disentangle landmark of unseen identity into two terms.

Landmark disentanglement

To decouple the identity and the expression geometry in a few-shot setting, we introduce a neural network to regress the coefficients for linear bases. Previously, such an approach has been widely used in modeling complex face geometries (Blanz and Vetter 1999). We separate expression landmarks into semantic groups of the face (e.g., mouth, nose and eyes) and perform PCA on each group to extract the expression bases from the training data:

$$\bar{\mathbf{l}}_{exp}(c, t) = \sum_{k=1}^{n_{exp}} \alpha_k(c, t)\mathbf{b}_{exp,k} = \mathbf{b}_{exp}^T \boldsymbol{\alpha}(c, t), \tag{5}$$

where $\mathbf{b}_{exp,k}$ and α_k represent the basis and the corresponding coefficient, respectively.

The proposed neural network, a *landmark disentangler* M, estimates $\boldsymbol{\alpha}(c, t)$ given an image $\mathbf{x}(c, t)$ and a landmark $\bar{\mathbf{l}}(c, t)$. Figure 5 illustrates the architecture of the landmark disentangler. Once the model is trained, the identity and the
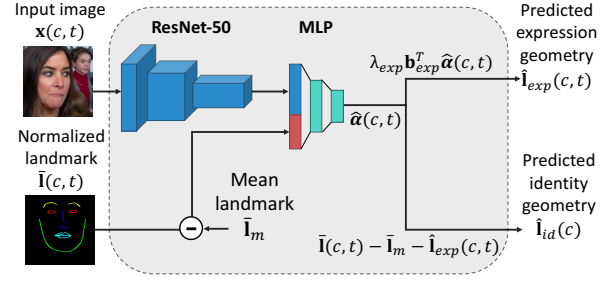

Figure 5: Architecture of landmark disentangler. Note that $\bar{\mathbf{l}}(c, t)$ is a set of landmark points but visualized as an image in the figure.

expression geometry can be computed as follows:

$$\begin{aligned}
\hat{\boldsymbol{\alpha}}(c, t) &= M\left(\mathbf{x}(c, t), \bar{\mathbf{l}}(c, t)\right) \\
\hat{\mathbf{l}}_{exp}(c, t) &= \lambda_{exp}\mathbf{b}_{exp}^T \hat{\boldsymbol{\alpha}}(c, t) \\
\hat{\mathbf{l}}_{id}(c) &= \bar{\mathbf{l}}(c, t) - \bar{\mathbf{l}}_m - \hat{\mathbf{l}}_{exp}(c, t),
\end{aligned} \tag{6}$$

where λ_{exp} is a hyperparameter that controls the intensity of the predicted expressions from the network. Image feature extracted by a ResNet-50 and the landmark, $\bar{\mathbf{l}}(c, t) - \bar{\mathbf{l}}_m$, are fed into a 2-layer MLP to predict $\hat{\boldsymbol{\alpha}}(c, t)$.

During the inference, the target and the driver landmarks are processed according to Equation 6. When multiple target images are given, we take the mean value over all $\hat{\mathbf{l}}_{id}(c_y)$. Finally, landmark transformer converts landmark as:

$$\hat{\mathbf{l}}(c_x \rightarrow c_y, t_x) = \bar{\mathbf{l}}_m + \hat{\mathbf{l}}_{id}(c_y) + \hat{\mathbf{l}}_{exp}(c_x, t_x). \tag{7}$$

Denormalization to recover the original scale, translation, and rotation is followed by the rasterization that generates a landmark adequate for the generator to consume. Further details of landmark transformer are described in Supplementary Material B.

Experimental Setup

Datasets We trained our model and the baselines using VoxCeleb1 (Nagrani, Chung, and Zisserman 2017), which contains 256×256 size videos of 1,251 different identities. We utilized the test split of VoxCeleb1 and CelebV (Wu et al. 2018) for evaluating self-reenactment and reenactment under a different identity, respectively. We created the test set by sampling 2,083 image sets from randomly selected 100 videos of VoxCeleb1 test split, and uniformly sampled 2,000 image sets from every identity from CelebV. The CelebV data includes the videos of five different celebrities of widely varying characteristics, which we utilize to evaluate the performance of the models reenacting unseen targets, similar to in-the-wild scenario. Further details of the loss function and the training method can be found at Supplementary Material A3 and A4.

Baselines MarioNETte variants, with and without the landmark transformer (*MarioNETte+LT* and *MarioNETte*, respectively), are compared with state-of-the-art models for

| Target | Driver | X2Face | Monkey-Net | NeuralHead-FF | MarioNETte | MarioNETte+LT |

Figure 6: Images generated by the proposed method and baselines, reenacting different identity on CelebV in one-shot setting.

few-shot face reenactment. Details of each baseline are as follows:

- **X2Face** (Wiles, Koepke, and Zisserman 2018). X2face utilizes direct image warping. We used the pre-trained model provided by the authors, trained on VoxCeleb1.

- **Monkey-Net** (Siarohin et al. 2019). Monkey-Net adopts feature-level warping. We used the implementation provided by the authors. Due to the structure of the method, Monkey-Net can only receive a single target image.

- **NeuralHead** (Zakharov et al. 2019). NeuralHead exploits AdaIN layers. Since a reference implementation is absent, we made an honest attempt to reproduce the results. Our implementation is a feed-forward version of their model (*NeuralHead-FF*) where we omit the meta-learning as well as fine-tuning phase, because we are interested in using a single model to deal with multiple identities.

Metrics We compare the models based on the following metrics to evaluate the quality of the generated images. Structured similarity (**SSIM**) (Wang et al. 2004) and peak signal-to-noise ratio (**PSNR**) evaluate the low-level similarity between the generated image and the ground-truth image. We also report the masked-SSIM (**M-SSIM**) and masked-PSNR (**M-PSNR**) where the measurements are restricted to the facial region.

In the absence of the ground truth image where different identity drives the target face, the following metrics are more relevant. Cosine similarity (**CSIM**) of embedding vectors generated by pre-trained face recognition model (Deng et al. 2019) is used to evaluate the quality of identity preservation. To inspect the capability of the model to properly reenact the pose and the expression of the driver, we com-

pute **PRMSE**, the root mean square error of the head pose angles, and **AUCON**, the ratio of identical facial action unit values, between the generated images and the driving images. OpenFace (Baltrusaitis et al. 2018) is utilized to compute pose angles and action unit values.

Experimental Results

Models were compared under self-reenactment and reenactment of different identities, including a user study. Ablation tests were conducted as well. All experiments were conducted under two different settings: one-shot and few-shot, where one or eight target images were used respectively.

Self-reenactment

Table 1 illustrates the evaluation results of the models under self-reenactment settings on VoxCeleb1. *MarioNETte* surpasses other models in every metric under few-shot setting and outperforms other models in every metric except for PSNR under the one-shot setting. However, *MarioNETte* shows the best performance in M-PSNR which implies that it performs better on facial region compared to baselines. The low CSIM yielded from *NeuralHead-FF* is an indirect evidence of the lack of capacity in AdaIN-based methods.

Reenacting Different Identity

Table 2 displays the evaluation result of reenacting a different identity on CelebV, and Figure 6 shows generated images from proposed method and baselines. *MarioNETte* and *MarioNETte+LT* preserve target identity adequately, thereby outperforming other models in CSIM. The proposed method alleviates the identity preservation problem regardless of the

Model (# target)	CSIM↑	SSIM↑	M-SSIM↑	PSNR↑	M-PSNR↑	PRMSE↓	AUCON↑
X2face (1)	0.689	0.719	0.941	22.537	31.529	3.26	0.813
Monkey-Net (1)	0.697	0.734	0.934	**23.472**	30.580	3.46	0.770
NeuralHead-FF (1)	0.229	0.635	0.923	20.818	29.599	3.76	0.791
MarioNETte (1)	**0.755**	**0.744**	**0.948**	23.244	**32.380**	**3.13**	**0.825**
X2face (8)	0.762	0.776	0.956	24.326	33.328	3.21	0.826
NeuralHead-FF (8)	0.239	0.645	0.925	21.362	29.952	3.69	0.795
MarioNETte (8)	**0.828**	**0.786**	**0.958**	**24.905**	**33.645**	**2.57**	**0.850**

Table 1: Evaluation result of self-reenactment setting on VoxCeleb1. Upward/downward pointing arrows correspond to metrics that are better when the values are higher/lower.

Model (# target)	CSIM↑	PRMSE↓	AUCON↑
X2face (1)	0.450	3.62	0.679
Monkey-Net (1)	0.451	4.81	0.584
NeuralHead-FF (1)	0.108	**3.30**	**0.722**
MarioNETte (1)	<u>0.520</u>	<u>3.41</u>	<u>0.710</u>
MarioNETte+LT (1)	**0.568**	3.70	0.684
X2face (8)	0.484	**3.15**	0.709
NeuralHead-FF (8)	0.120	<u>3.26</u>	**0.723**
MarioNETte (8)	<u>0.608</u>	<u>3.26</u>	<u>0.717</u>
MarioNETte+LT (8)	**0.661**	3.57	0.691

Table 2: Evaluation result of reenacting a different identity on CelebV. **Bold** and <u>underlined</u> values correspond to the best and the second-best value of each metric, respectively.

Model (# target)	vs. Ours	vs. Ours+LT	Realism ↑
X2Face (1)	0.07	0.09	0.093
Monkey-Net (1)	0.05	0.09	0.100
NeuralHead-FF (1)	0.17	0.17	0.087
MarioNETte (1)	-	0.51	0.140
MarioNETte+LT (1)	-	-	**0.187**
X2Face (8)	0.09	0.07	0.047
NeuralHead-FF (8)	0.15	0.16	0.080
MarioNETte (8)	-	0.52	0.147
MarioNETte+LT (8)	-	-	**0.280**

Table 3: User study results of reenacting different identity on CelebV. *Ours* stands for our proposed model, *MarioNETte*, and *Ours+LT* stands for *MarioNETte+LT*.

driver being of the same identity or not. While *NeuralHead-FF* exhibits slightly better performance in terms of PRMSE and AUCON compared to *MarioNETte*, the low CSIM of *NeuralHead-FF* portrays the failure to preserve the target identity. The landmark transformer significantly boosts identity preservation at the cost of a slight decrease in PRMSE and AUCON. The decrease may be due to the PCA bases for the expression disentanglement not being diverse enough to span the whole space of expressions. Moreover, the disentanglement of identity and expression itself is a non-trivial problem, especially in a one-shot setting.

User Study

Two types of user studies are conducted to assess the performance of the proposed model:

- **Comparative analysis.** Given three example images of the target and a driver image, we displayed two images generated by different models and asked human evaluators to select an image with higher quality. The users were asked to assess the quality of an image in terms of (1) identity preservation, (2) reenactment of driver's pose and expression, and (3) photo-realism. We report the winning ratio of baseline models compared to our proposed models. We believe that user reported score better reflects the quality of different models than other indirect metrics.

- **Realism analysis.** Similar to the user study protocol of Zakharov et al. (2019), three images of the same person,

where two of the photos were taken from a video and the remaining generated by the model, were presented to human evaluators. Users were instructed to choose an image that differs from the other two in terms of the identity under a three-second time limit. We report the ratio of deception, which demonstrates the identity preservation and the photo-realism of each model.

For both studies, 150 examples were sampled from CelebV, which were evenly distributed to 100 different human evaluators.

Table 3 illustrates that our models are preferred over existing methods achieving realism scores with a large margin. The result demonstrates the capability of *MarioNETte* in creating photo-realistic reenactments while preserving the target identity in terms of human perception. We see a slight preference of *MarioNETte* over *MarioNETte+LT*, which agrees with the Table 2, as *MarioNETte+LT* has better identity preservation capability at the expense of slight degradation in expression transfer. Since the identity preservation capability of *MarioNETte+LT* surpasses all other models in realism score, almost twice the score of even *MarioNETte* on few-shot settings, we consider the minor decline in expression transfer a good compromise.

Model (# target)	CSIM↑	PRMSE↓	AUCON↑
AdaIN (1)	0.063	3.47	0.724
+Attention (1)	0.333	**3.17**	**0.729**
+Alignment (1)	**0.530**	3.44	0.700
MarioNETte (1)	0.520	3.41	0.710
AdaIN (8)	0.069	3.40	0.723
+Attention (8)	0.472	**3.22**	**0.727**
+Alignment (8)	0.605	3.27	0.709
MarioNETte (8)	**0.608**	3.26	0.717

Table 4: Comparison of ablation models for reenacting different identity on CelebV.
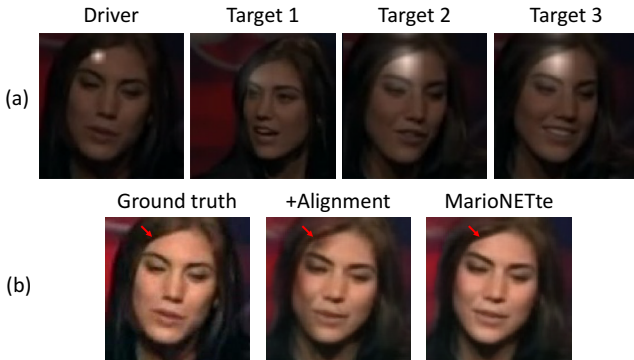

Figure 7: (a) Driver and target images overlapped with attention map. Brightness signifies the intensity of the attention. (b) Failure case of *+Alignment* and improved result generated by *MarioNETte*.

Ablation Test

We performed ablation test to investigate the effectiveness of the proposed components. While keeping all other things the same, we compare the following configurations reenacting different identities: (1) **MarioNETte** is the proposed method where both image attention block and target feature alignment are applied. (2) **AdaIN** corresponds to the same model as MarioNETte, where the image attention block is replaced with AdaIN residual block while the target feature alignment is omitted. (3) **+Attention** is a MarioNETte where only the image attention block is applied. (4) **+Alignment** only employs the target feature alignment.

Table 4 shows result of ablation test. For identity preservation (i.e., CSIM), *AdaIN* has a hard time combining style features depending solely on AdaIN residual blocks. *+Attention* alleviates the problem immensely in both one-shot and few-shot settings by attending to proper coordinates. While *+Alignment* exhibits a higher CSIM compared to *+Attention*, it struggles in generating plausible images for unseen poses and expressions leading to worse PRMSE and AUCON. Taking advantage of both attention and target feature alignment, *MarioNETte* outperforms *+Alignment* in every metric under consideration.

Entirely relying on target feature alignment for reenact-

ment, *+Alignment* is vulnerable to failures due to large differences in pose between target and driver that *MarioNETte* can overcome. Given a single driver image along with three target images (Figure 7a), *+Alignment* has defects on the forehead (denoted by arrows in Figure 7b). This is due to (1) warping low-level features from a large-pose input and (2) aggregating features from multiple targets with diverse poses. *MarioNETte*, on the other hand, gracefully handles the situation by attending to proper image among several target images as well as adequate spatial coordinates in the target image. The attention map, highlighting the area where the image attention block is focusing on, is illustrated with white in Figure 7a. Note that *MarioNETte* attends to the forehead and adequate target images (Target 2 and 3 in Figure 7a) which has similar pose with driver.

Related Works

The classical approach to face reenactment commonly involves the use of explicit 3D modeling of human faces (Blanz and Vetter 1999) where the 3DMM parameters of the driver and the target are computed from a single image, and blended eventually (Thies et al. 2015; Thies et al. 2016). Image warping is another popular approach where the target image is modified using the estimated flow obtained form 3D models (Cao et al. 2013) or sparse landmarks (Averbuch-Elor et al. 2017). Face reenactment studies have embraced the recent success of neural networks exploring different image-to-image translation architectures (Isola et al. 2017) such as the works of Xu et al. (2017) and that of Wu et al. (2018), which combined the cycle consistency loss (Zhu et al. 2017). A hybrid of two approaches has been studied as well. Kim et al. (2018) trained an image translation network which maps reenacted render of a 3D face model into a photo-realistic output.

Architectures, capable of blending the style information of the target with the spatial information of the driver, have been proposed recently. AdaIN (Huang and Belongie 2017; Huang et al. 2018; Liu et al. 2019) layer, attention mechanism (Zhu et al. 2019; Lathuilière et al. 2019; Park and Lee 2019), deformation operation (Siarohin et al. 2018; Dong et al. 2018), and GAN-based method (Bao et al. 2018) have all seen a wide adoption. Similar idea has been applied to few-shot face reenactment settings such as the use of image-level (Wiles, Koepke, and Zisserman 2018) and feature-level (Siarohin et al. 2019) warping, and AdaIN layer in conjuction with a meta-learning (Zakharov et al. 2019). The identity mismatch problem has been studied through methods such as CycleGAN-based landmark transformers (Wu et al. 2018) and landmark swappers (Zhang et al. 2019). While effective, these methods either require an independent model per person or a dataset with image pairs that may be hard to acquire.

Conclusions

In this paper, we have proposed a framework for few-shot face reenactment. Our proposed image attention block and target feature alignment, together with the landmark transformer, allow us to handle the identity mismatch caused by

using the landmarks of a different person. Proposed method do not need additional fine-tuning phase for identity adaptation, which significantly increases the usefulness of the model when deployed in-the-wild. Our experiments including human evaluation suggest the excellence of the proposed method.

One exciting avenue for future work is to improve the landmark transformer to better handle the landmark disentanglement to make the reenactment even more convincing.

References

[Averbuch-Elor et al. 2017] Averbuch-Elor, H.; Cohen-Or, D.; Kopf, J.; and Cohen, M. F. 2017. Bringing portraits to life. *ACM Transactions on Graphics* 36(6):196.

[Balakrishnan et al. 2018] Balakrishnan, G.; Zhao, A.; Dalca, A. V.; Durand, F.; and Guttag, J. 2018. Synthesizing images of humans in unseen poses. In *Proceedings of the IEEE/CVF Conference on Computer Vision and Pattern Recognition*, 8340–8348.

[Baltrusaitis et al. 2018] Baltrusaitis, T.; Zadeh, A.; Lim, Y. C.; and Morency, L.-P. 2018. Openface 2.0: Facial behavior analysis toolkit. In *Proceedings of the International Conference on Automatic Face and Gesture Recognition*, 59–66.

[Bao et al. 2018] Bao, J.; Chen, D.; Wen, F.; Li, H.; and Hua, G. 2018. Towards open-set identity preserving face synthesis. In *Proceedings of the IEEE Conference on Computer Vision and Pattern Recognition*, 6713–6722.

[Blanz and Vetter 1999] Blanz, V., and Vetter, T. 1999. A morphable model for the synthesis of 3d faces. In *Proceedings of the ACM SIGGRAPH Conference on Computer Graphics*, volume 99, 187–194.

[Brock, Donahue, and Simonyan 2019] Brock, A.; Donahue, J.; and Simonyan, K. 2019. Large scale GAN training for high fidelity natural image synthesis. In *Proceedings of International Conference on Learning and Representation*.

[Bulat and Tzimiropoulos 2017] Bulat, A., and Tzimiropoulos, G. 2017. How far are we from solving the 2d & 3d face alignment problem? (and a dataset of 230,000 3d facial landmarks). In *Proceedings of the International Conference on Computer Vision*.

[Cao et al. 2013] Cao, C.; Weng, Y.; Zhou, S.; Tong, Y.; and Zhou, K. 2013. Facewarehouse: A 3d facial expression database for visual computing. *IEEE Transactions on Visualization and Computer Graphics* 20(3):413–425.

[Deng et al. 2019] Deng, J.; Guo, J.; Xue, N.; and Zafeiriou, S. 2019. Arcface: Additive angular margin loss for deep face recognition. In *Proceedings of the IEEE/CVF Conference on Computer Vision and Pattern Recognition*, 4690–4699.

[Dong et al. 2018] Dong, H.; Liang, X.; Gong, K.; Lai, H.; Zhu, J.; and Yin, J. 2018. Soft-gated warping-gan for pose-guided person image synthesis. In *Advances in Neural Information Processing Systems*, 474–484.

[He et al. 2016] He, K.; Zhang, X.; Ren, S.; and Sun, J. 2016. Deep residual learning for image recognition. In *Proceedings of the IEEE conference on computer vision and pattern recognition*, 770–778.

[Huang and Belongie 2017] Huang, X., and Belongie, S. 2017. Arbitrary style transfer in real-time with adaptive instance normalization. In *Proceedings of the International Conference on Computer Vision*, 1501–1510.

[Huang et al. 2018] Huang, X.; Liu, M.-Y.; Belongie, S.; and Kautz, J. 2018. Multimodal unsupervised image-to-image translation. In *Proceedings of the European Conference on Computer Vision*, 172–189.

[Isola et al. 2017] Isola, P.; Zhu, J.-Y.; Zhou, T.; and Efros, A. A. 2017. Image-to-image translation with conditional adversarial networks. In *Proceedings of the IEEE/CVF Conference on Computer Vision and Pattern Recognition*, 1125–1134.

[Jaderberg et al. 2015] Jaderberg, M.; Simonyan, K.; Zisserman, A.; et al. 2015. Spatial transformer networks. In *Advances in Neural Information Processing Systems*, 2017–2025.

[Johnson, Alahi, and Fei-Fei 2016] Johnson, J.; Alahi, A.; and Fei-Fei, L. 2016. Perceptual losses for real-time style transfer and super-resolution. In *Proceedings of the European Conference on Computer Vision*, 694–711.

[Kim et al. 2018] Kim, H.; Carrido, P.; Tewari, A.; Xu, W.; Thies, J.; Niessner, M.; Pérez, P.; Richardt, C.; Zollhöfer, M.; and Theobalt, C. 2018. Deep video portraits. *ACM Transactions on Graphics* 37(4):163.

[Lathuilière et al. 2019] Lathuilière, S.; Sangineto, E.; Siarohin, A.; and Sebe, N. 2019. Attention-based fusion for multi-source human image generation. *arXiv preprint arXiv:1905.02655*.

[Lim and Ye 2017] Lim, J. H., and Ye, J. C. 2017. Geometric gan. *arXiv preprint arXiv:1705.02894*.

[Liu et al. 2019] Liu, M.-Y.; Huang, X.; Mallya, A.; Karras, T.; Aila, T.; Lehtinen, J.; and Kautz, J. 2019. Few-shot unsupervised image-to-image translation. *arXiv preprint arXiv:1905.01723*.

[Miyato and Koyama 2018] Miyato, T., and Koyama, M. 2018. cgans with projection discriminator. *arXiv preprint arXiv:1802.05637*.

[Miyato et al. 2018] Miyato, T.; Kataoka, T.; Koyama, M.; and Yoshida, Y. 2018. Spectral normalization for generative adversarial networks. In *Proceedings of International Conference on Learning and Representation*.

[Nagrani, Chung, and Zisserman 2017] Nagrani, A.; Chung, J. S.; and Zisserman, A. 2017. Voxceleb: a large-scale speaker identification dataset. *Proceedings of the Annual Conference of the International Speech Communication Association*.

[Park and Lee 2019] Park, D. Y., and Lee, K. H. 2019. Arbitrary style transfer with style-attentional networks. In *Proceedings of the IEEE/CVF Conference on Computer Vision and Pattern Recognition*, 5880–5888.

[Parkhi, Vedaldi, and Zisserman 2015] Parkhi, O. M.; Vedaldi, A.; and Zisserman, A. 2015. Deep face recognition. In *Proceedings of the British Machine Vision Conference*, 41.1–41.12.

[Ronneberger, Fischer, and Brox 2015] Ronneberger, O.; Fischer, P.; and Brox, T. 2015. U-Net: Convolutional networks for biomedical image segmentation. In *Proceedings of the International Conference on Medical Image Computing and Computer Assisted Intervention*.

[Siarohin et al. 2018] Siarohin, A.; Sangineto, E.; Lathuilière, S.; and Sebe, N. 2018. Deformable gans for pose-based human image generation. In *Proceedings of the IEEE/CVF Conference on Computer Vision and Pattern Recognition*, 3408–3416.

[Siarohin et al. 2019] Siarohin, A.; Lathuilire, S.; Tulyakov, S.; Ricci, E.; and Sebe, N. 2019. Animating arbitrary objects via deep motion transfer. In *Proceedings of the IEEE/CVF Conference on Computer Vision and Pattern Recognition*.

[Simonyan and Zisserman 2014] Simonyan, K., and Zisserman, A. 2014. Very deep convolutional networks for large-scale image recognition. *arXiv preprint arXiv:1409.1556*.

[Thies et al. 2015] Thies, J.; Zollhöfer, M.; Nießner, M.; Valgaerts, L.; Stamminger, M.; and Theobalt, C. 2015. Real-time expression transfer for facial reenactment. *ACM Transactions on Graphics* 34(6):183–1.

[Thies et al. 2016] Thies, J.; Zollhofer, M.; Stamminger, M.; Theobalt, C.; and Nießner, M. 2016. Face2face: Real-time face capture and reenactment of rgb videos. In *Proceedings of the IEEE/CVF Conference on Computer Vision and Pattern Recognition*, 2387–2395.

[Vaswani et al. 2017] Vaswani, A.; Shazeer, N.; Parmar, N.; Uszkoreit, J.; Jones, L.; Gomez, A. N.; Kaiser, Ł.; and Polosukhin, I. 2017. Attention is all you need. In *Advances in Neural Information Processing Systems*, 5998–6008.

[Wang et al. 2004] Wang, Z.; Bovik, A. C.; Sheikh, H. R.; Simoncelli, E. P.; et al. 2004. Image quality assessment: from error visibility to structural similarity. *IEEE Transactions on Image Processing* 13(4):600–612.

[Wiles, Koepke, and Zisserman 2018] Wiles, O.; Koepke, A. S.; and Zisserman, A. 2018. X2face: A network for controlling face generation by using images, audio, and pose codes. In *Proceedings of the European Conference on Computer Vision*.

[Wu et al. 2018] Wu, W.; Zhang, Y.; Li, C.; Qian, C.; and Change Loy, C. 2018. Reenactgan: Learning to reenact faces via boundary transfer. In *Proceedings of the European Conference on Computer Vision*, 603–619.

[Xu et al. 2017] Xu, R.; Zhou, Z.; Zhang, W.; and Yu, Y. 2017. Face transfer with generative adversarial network. *arXiv preprint arXiv:1710.06090*.

[Zakharov et al. 2019] Zakharov, E.; Shysheya, A.; Burkov, E.; and Lempitsky, V. 2019. Few-shot adversarial learning of realistic neural talking head models. *arXiv preprint arXiv:1905.08233*.

[Zhang et al. 2019] Zhang, J.; Zeng, X.; Pan, Y.; Liu, Y.; Ding, Y.; and Fan, C. 2019. Faceswapnet: Landmark guided many-to-many face reenactment. *arXiv preprint arXiv:1905.11805*.

[Zhu et al. 2017] Zhu, J.-Y.; Park, T.; Isola, P.; and Efros, A. A. 2017. Unpaired image-to-image translation using cycle-consistent adversarial networks. In *Proceedings of the IEEE/CVF Conference on Computer Vision and Pattern Recognition*, 2223–2232.

[Zhu et al. 2019] Zhu, Z.; Huang, T.; Shi, B.; Yu, M.; Wang, B.; and Bai, X. 2019. Progressive pose attention transfer for person image generation. In *Proceedings of the IEEE/CVF Conference on Computer Vision and Pattern Recognition*, 2347–2356.

MarioNETte Architecture Details

Architecture design

Given a driver image $\mathbf{x}$ and K target images $\{\mathbf{y}^i\}_{i=1...K}$, the proposed few-shot face reenactment framework which we call *MarioNETte* first generates 2D landmark images (i.e. $\mathbf{r}_x$ and $\{\mathbf{r}_y^i\}_{i=1...K}$). We utilize a *3D landmark detector* $\mathcal{K} : \mathbb{R}^{h \times w \times 3} \rightarrow \mathbb{R}^{68 \times 3}$ (Bulat and Tzimiropoulos 2017) to extract facial keypoints which includes information about pose and expression denoted as $\mathbf{l}_x = \mathcal{K}(\mathbf{x})$ and $\mathbf{l}_y^i = \mathcal{K}(\mathbf{y}^i)$, respectively. We further rasterize 3D landmarks to an image by rasterizer $\mathcal{R}$, resulting in $\mathbf{r}_x = \mathcal{R}(\mathbf{l}_x), \mathbf{r}_y^i = \mathcal{R}(\mathbf{l}_y^i)$.

We utilize simple rasterizer that orthogonally projects 3D landmark points, e.g., (x, y, z), into 2D XY-plane, e.g., (x, y), and we group the projected landmarks into 8 categories: left eye, right eye, contour, nose, left eyebrow, right eyebrow, inner mouth, and outer mouth. For each group, lines are drawn between predefined order of points with predefined colors (e.g., red, red, green, blue, yellow, yellow, cyan, and cyan respectively), resulting in a rasterized image as shown in Figure 8.
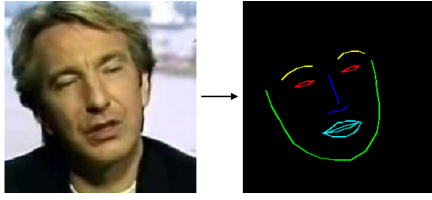

Figure 8: Example of the rasterized facial landmarks.

MarioNETte consists of **conditional image generator** $G(\mathbf{r}_x; \{\mathbf{y}^i\}_{i=1...K}, \{\mathbf{r}_y^i\}_{i=1...K})$ and **projection discriminator** $D(\hat{\mathbf{x}}, \hat{\mathbf{r}}, c)$. The discriminator D determines whether the given image $\hat{\mathbf{x}}$ is a real image from the data distribution taking into account the conditional input of the rasterized landmarks $\hat{\mathbf{r}}$ and identity c.

The **generator** $G(\mathbf{r}_x; \{\mathbf{y}^i\}_{i=1...K}, \{\mathbf{r}_y^i\}_{i=1...K})$ is further broken down into four components: namely, *target encoder*, *drvier encoder*, *blender*, and *decoder*. *Target encoder* $E_y(\mathbf{y}, \mathbf{r}_y)$ takes target image and generates encoded target feature map $\mathbf{z}_y$ together with the warped target feature map $\hat{\mathbf{S}}$. *Driver encoder* $E_x(\mathbf{r}_x)$ receives a driver image and creates a driver feature map $\mathbf{z}_x$. *Blender* $B(\mathbf{z}_x, \{\mathbf{z}_y^i\}_{i=1...K})$ combines encoded feature maps to produce a mixed feature map $\mathbf{z}_{xy}$. *Decoder* $Q(\mathbf{z}_{xy}, \{\hat{\mathbf{S}}^i\}_{i=1...K})$ generates the reenacted image. Input image $\mathbf{y}$ and the landmark image $\mathbf{r}_y$ are concatenated channel-wise and fed into the target encoder.

The **target encoder** $E_y(\mathbf{y}, \mathbf{r}_y)$ adopts a U-Net (Ronneberger, Fischer, and Brox 2015) style architecture including five downsampling blocks and four upsampling blocks with skip connections. Among five feature maps $\{\mathbf{s}_j\}_{j=1...5}$ generated by the downsampling blocks, the most downsampled feature map, $\mathbf{s}_5$, is used as the encoded target feature map $\mathbf{z}_y$, while the others, $\{\mathbf{s}_j\}_{j=1...4}$, are transformed into normalized feature maps. A normalization flow map $\mathbf{f}_y \in \mathbb{R}^{(h/2) \times (w/2) \times 2}$ transforms each feature map into normalized feature map, $\hat{\mathbf{S}} = \{\hat{\mathbf{s}}_j\}_{j=1...4}$, through warping function $\mathcal{T}$ as follows:

$$\hat{\mathbf{S}} = \{\mathcal{T}(\mathbf{s}_1; \mathbf{f}_y), \dots, \mathcal{T}(\mathbf{s}_4; \mathbf{f}_y)\}. \tag{8}$$

Flow map $\mathbf{f}_y$ is generated at the end of upsampling blocks followed by an additional convolution layer and a hyperbolic tangent activa-

tion layer, thereby producing a 2-channel feature map, where each channel denotes a flow for the horizontal and vertical direction, respectively.

We adopt bilinear sampler based warping function which is widely used along with neural networks due to its differentiability (Jaderberg et al. 2015; Balakrishnan et al. 2018; Siarohin et al. 2019). Since each $\mathbf{s}_j$ has a different width and height, average pooling is applied to downsample $\mathbf{f}_y$ to match the size of $\mathbf{f}_y$ to that of $\mathbf{s}_j$.

The **driver encoder** $E_x(\mathbf{r}_x)$, which consists of four residual downsampling blocks, takes driver landmark image $\mathbf{r}_x$ and generates driver feature map $\mathbf{z}_x$.

The **blender** $B(\mathbf{z}_x, \{\mathbf{z}_y^i\}_{i=1...K})$ produces mixed feature map $\mathbf{z}_{xy}$ by blending the positional information of $\mathbf{z}_x$ with the target style feature maps $\mathbf{z}_y$. We stacked three *image attention blocks* to build our blender.

The **decoder** $Q(\mathbf{z}_{xy}, \{\hat{\mathbf{S}}^i\}_{i=1...K})$ consists of four *warp-alignment blocks* followed by residual upsampling blocks. Note that the last upsampling block is followed by an additional convolution layer and a hyperbolic tangent activation function.

The **discriminator** $D(\hat{\mathbf{x}}, \hat{\mathbf{r}}, c)$ consists of five residual downsampling blocks without self-attention layers. We adopt a projection discriminator with a slight modification of removing the global sum-pooling layer from the original structure. By removing the global sum-pooling layer, discriminator generates scores on multiple patches like PatchGAN discriminator (Isola et al. 2017).

We adopt the residual upsampling and downsampling block proposed by Brock, Donahue, and Simonyan (2019) to build our networks. All batch normalization layers are substituted with instance normalization except for the target encoder and the discriminator, where the normalization layer is absent. We utilized ReLU as an activation function. The number of channels is doubled (or halved) when the output is downsampled (or upsampled). The minimum number of channels is set to 64 and the maximum number of channels is set to 512 for every layer. Note that the input image, which is used as an input for the target encoder, driver encoder, and discriminator, is first projected through a convolutional layer to match the channel size of 64.

Positional encoding

We utilize a sinusoidal positional encoding introduced by Vaswani et al. (2017) with a slight modification. First, we divide the number of channels of the positional encoding in half. Then, we utilize half of them to encode the horizontal coordinate and the rest of them to encode the vertical coordinate. To encode the relative position, we normalize the absolute coordinate by the width and the height of the feature map. Thus, given a feature map of $\mathbf{z} \in \mathbb{R}^{h_z \times w_z \times c_z}$, the corresponding positional encoding $\mathbf{P} \in \mathbb{R}^{h_z \times w_z \times c_z}$ is computed as follows:

$$
\begin{aligned}
\mathbf{P}_{i,j,4k} &= \sin\left(\frac{256i}{h_z \cdot 10000^{2k/c_z}}\right) \\
\mathbf{P}_{i,j,4k+1} &= \cos\left(\frac{256i}{h_z \cdot 10000^{2k/c_z}}\right) \\
\mathbf{P}_{i,j,4k+2} &= \sin\left(\frac{256j}{w_z \cdot 10000^{2k/c_z}}\right) \\
\mathbf{P}_{i,j,4k+3} &= \cos\left(\frac{256j}{w_z \cdot 10000^{2k/c_z}}\right).
\end{aligned}
\tag{9}
$$

Loss functions

Our model is trained in an adversarial manner using a projection discriminator D (Miyato and Koyama 2018). The discriminator

aims to distinguish between the real image of the identity c and a synthesized image of c generated by G. Since the paired target and the driver images from different identities cannot be acquired without explicit annotation, we trained our model using the target and the driver image extracted from the same video. Thus, identities of $\mathbf{x}$ and $\mathbf{y}^i$ are always the same, e.g., c, for every target and driver image pair, i.e., $(\mathbf{x}, \{\mathbf{y}^i\}_{i=1...K})$, during the training.

We use hinge GAN loss (Lim and Ye 2017) to optimize discriminator D as follows:

$$
\begin{aligned}
\hat{\mathbf{x}} =\ & G(\mathbf{r}_x; \{\mathbf{y}^i\}, \{\mathbf{r}_y^i\}) \\
\mathcal{L}_D =\ & \max(0, 1 - D(\mathbf{x}, \mathbf{r}_x, c)) \quad + \\
& \max(0, 1 + D(\hat{\mathbf{x}}, \mathbf{r}_x, c)).
\end{aligned} \tag{10}
$$

The loss function of the generator consists of four components including the GAN loss $\mathcal{L}_{GAN}$, the perceptual losses ($\mathcal{L}_P$ and $\mathcal{L}_{PF}$), and the feature matching loss $\mathcal{L}_{FM}$. The GAN loss $\mathcal{L}_{GAN}$ is a generator part of the hinge GAN loss and defined as follows:

$$
\mathcal{L}_{GAN} = -D(\hat{\mathbf{x}}, \mathbf{r}_x, c). \tag{11}
$$

The perceptual loss (Johnson, Alahi, and Fei-Fei 2016) is calculated by averaging L_1-distances between the intermediate features of the pre-trained network using ground truth image $\mathbf{x}$ and the generated image $\hat{\mathbf{x}}$. We use two different networks for perceptual losses where $\mathcal{L}_P$ and $\mathcal{L}_{PF}$ are extracted from VGG19 and VGG-VD-16 each trained for ImageNet classification task (Simonyan and Zisserman 2014) and a face recognition task (Parkhi, Vedaldi, and Zisserman 2015), respectively. We use features from the following layers to compute the perceptual losses: relu1_1, relu2_1, relu3_1, relu4_1, and relu5_1. Feature matching loss $\mathcal{L}_{FM}$ is the sum of L_1-distances between the intermediate features of the discriminator D when processing the ground truth image $\mathbf{x}$ and the generated image $\hat{\mathbf{x}}$ which helps with the stabilization of the adversarial training. It helps to stabilize the adversarial training. The overall generator loss is the weighted sum of the four losses:

$$
\mathcal{L}_G = \mathcal{L}_{GAN} + \lambda_P \mathcal{L}_P + \lambda_{PF} \mathcal{L}_{PF} + \lambda_{FM} \mathcal{L}_{FM}. \tag{12}
$$

Training details

To stabilize the adversarial training, we apply spectral normalization (Miyato et al. 2018) for every layer of the discriminator and the generator. In addition, we use the convex hull of the facial landmarks as a facial region mask and give three-fold weights to the corresponding masked position while computing the perceptual loss. We use Adam optimizer to train our model where the learning rate of 2×10^{-4} is used for the discriminator and 5×10^{-5} is used for the generator and the style encoder. Unlike the setting of Brock, Donahue, and Simonyan (2019), we only update the discriminator once per every generator updates. We set λ_P to 10, λ_{PF} to 0.01, λ_{FM} to 10, and the number of target images K to 4 during the training.

Landmark Transformer Details
Landmark decomposition
Formally, landmark decomposition is calculated as:

$$
\begin{aligned}
\bar{\mathbf{l}}_m &= \frac{1}{CT} \sum_c \sum_t \bar{\mathbf{l}}(c, t), \\
\bar{\mathbf{l}}_{id}(c) &= \frac{1}{T_c} \sum_t \bar{\mathbf{l}}(c, t) - \bar{\mathbf{l}}_m, \\
\bar{\mathbf{l}}_{exp}(c, t) &= \bar{\mathbf{l}}(c, t) - \bar{\mathbf{l}}_m - \bar{\mathbf{l}}_{id}(c) \\
&= \bar{\mathbf{l}}(c, t) - \frac{1}{T_c} \sum_t \bar{\mathbf{l}}(c, t),
\end{aligned} \tag{13}
$$

where C is the number of videos, T_c is the number of frames of c-th video, and $T = \sum T_c$. We can easily compute the components shown in Equation 13 from the training dataset.

However, when an image of unseen identity c' is given, the decomposition of the identity and the expression shown in Equation 13 is not possible since $\bar{\mathbf{l}}_{exp}(c', t)$ will be zero for a single image. Even when a few frames of an unseen identity c' is given, $\bar{\mathbf{l}}_{exp}(c', t)$ will be zero (or near zero) if the expressions in the given frames are not diverse enough. Thus, to perform the decomposition shown in Equation 13 even under the one-shot or few-shot settings, we introduce *landmark disentangler*.

Landmark disentanglement

To compute the expression basis $\mathbf{b}_{exp}$, using the expression geometry obtained from the VoxCeleb1 training data, we divide a landmark into different groups (e.g., left eye, right eye, eyebrows, mouth, and any other) and perform PCA on each group. We utilize PCA dimensions of 8, 8, 8, 16 and 8, for each group, resulting in a total number of expression bases, n_{exp}, of 48.

We train landmark disentangler on the VoxCeleb1 training set, separately. Before training landmark disentangler, we normalized each expression parameter α_i to follow a standard normal distribution $\mathcal{N}(0, 1^2)$ for the ease of regression training. We employ ResNet50, which is pre-trained on ImageNet (He et al. 2016), and extract features from the first layer to the last layer right before the global average pooling layer. Extracted image features are concatenated with the normalized landmark $\bar{\mathbf{l}}$ subtracted by the mean landmark $\bar{\mathbf{l}}_m$, and fed into a 2-layer MLP followed by a ReLU activation. The whole network is optimized by minimizing the MSE loss between the predicted expression parameters and the target expression parameters, using Adam optimizer with a learning rate of 3×10^{-4}. We use gradient clipping with the maximum gradient norm of 1 during the training. We set the expression intensity parameter λ_{exp} to 1.5.

Additional Ablation Tests
Quantitative results

In Table 1 and Table 2 of the main paper, *MarioNETte* shows better PRMSE and AUCON under the self-reenactment setting on VoxCeleb1 compared to *NeuralHead-FF*, which, however, is reversed under the reenactment of a different identity on CelebV. We provide an explanation of this phenomenon through an ablation study.

Table 5 illustrates the evaluation results of ablation models under self-reenactment settings on VoxCeleb1. Unlike the evaluation results of reenacting a different identity on CelebV (Table 4 of the main paper), +*Alignment* and *MarioNETte* show better PRMSE and AUCON compared to the *AdaIN*. The phenomenon may be attributed to the characteristics of the training dataset as well as the different inductive biases of different models. VoxCeleb1 consists of short video clips (usually 5-10s long), leading to similar poses and expressions between drivers and targets. Unlike the AdaIN-based model which is unaware of spatial information, the proposed image attention block and the target feature alignment encode spatial information from the target image. We suspect that this may lead to possible overfitting of the proposed model to the *same identity pair with a similar pose and expression* setting.

Qualitative results

Figure 9 and Figure 10 illustrate the results of ablation models reenacting a different identity on CelebV under the one-shot and few-shot settings, respectively. While *AdaIN* fails to generate an image that resembles the target identity, +*Attention* successfully maintains the key characteristics of the target. The target feature

Model (# target)	CSIM↑	PRMSE↓	AUCON↑
AdaIN (1)	0.183	3.719	0.781
+Attention (1)	0.611	3.257	<u>0.825</u>
+Alignment (1)	**0.756**	**3.069**	**0.827**
MarioNETte (1)	<u>0.755</u>	<u>3.125</u>	<u>0.825</u>
AdaIN (8)	0.188	3.649	0.787
+Attention (8)	0.717	2.909	0.843
+Alignment (8)	<u>0.826</u>	**2.563**	<u>0.845</u>
MarioNETte (8)	**0.828**	<u>2.571</u>	**0.850**

Table 5: Comparison of ablation models for self-reenactment setting on VoxCeleb1 dataset.

alignment module adds fine-grained details to the generated image. However, *MarioNETte* tends to generate more natural images in a few-shot setting, while *+Alignment* struggles to deal with multiple target images with diverse poses and expressions.

Inference Time

In this section, we report the inference time of our model. We measured the latency of the proposed method while generating 256×256 images with different number of target images, K $\in \{1, 8\}$. We ran each setting for 300 times and report the average speed. We utilized *Nvidia Titan Xp* and *Pytorch 1.0.1.post2*. As mentioned in the main paper, we used the open-sourced implementation of Bulat and Tzimiropoulos (2017) to extract 3D facial landmarks.

Table 6 displays the inference time breakdown of our models. Total inference time of the proposed models, *MarioNETte+LT* and *MarioNETte*, can be derived as shown in Table 7. While generating reenactment videos, z_y and $\hat{\mathbf{S}}$, utilized to compute the target encoding, is generated only once at the beginning. Thus, we divide our inference pipeline into *Target encoding* part and the *Driver generation* part.

Since we perform a batched inference for multiple target images, the inference time of the proposed components (e.g., the target encoder and the target landmark transformer) scale sublinearly to the number of target images K. On the other hand, the open-source 3D landmark detector processes images in a sequential manner, and thus, its processing time scales linearly.

Additional Examples of Generated Images

We provide additional qualitative results of the baseline methods and the proposed models on VoxCeleb1 and CelebV datasets. We report the qualitative results for both one-shot and few-shot (8 target images) settings, except *Monkey-Net* which is designed for using only a single image. In the case of the few-shot reenactment, we display only one target image, due to the limited space.

Figure 11 and Figure 12 compare different methods for the self-reenactment on VoxCeleb1 in one-shot and few-shot settings, respectively. Examples of one-shot and few-shot reenactments on VoxCeleb1 where driver's and target's identity do not match is shown in Figures 13 and Figure 14, respectively.

Figure 15, Figure 16, and Figure 17 depict the qualitative results on the CelebV dataset. One-shot and few-shot self-reenactment settings of various methods are compared in Figures 15 and Figure 16, respectively. The results of reenacting a different identity on CelebV under the few-shot setting can be found in Figure 17.

Figure 18 reveals failure cases generated by *MarioNETte+LT* while performing a one-shot reenactment under different identity setting on VoxCeleb1. Large pose difference between the driver and the target seems to be the main reason for the failures.

Description	Symbol	Inference time (ms)
3D Landmark Detector	T_P	101
Target Encoder	$T_{E,K}$	44 (K=1), 111 (K=8)
Target Landmark Transformer	$T_{TLT,K}$	22 (K=1), 19 (K=8)
Generator	$T_{G,K}$	35 (K=1), 36 (K=8)
Driver Landmark Transformer	T_{DLT}	26

Table 6: Inference speed of each component of our model.

Model	Target encoding	Driver generation
MarioNETte+LT	$K \cdot T_P + T_{TLT,K} + T_{E,K}$	$T_P + T_{DLT} + T_{G,K}$
MarioNETte	$K \cdot T_P + T_{E,K}$	$T_P + T_{G,K}$

Table 7: Inference speed of the full model for generating single image with K target images.

Figure 9: Qualitative results of ablation models of one-shot reenactment under different identity setting on CelebV.

Figure 10: Qualitative results of ablation models of few-shot reenactment under different identity setting on CelebV.

| Target | Driver | X2Face | Monkey-Net | NeuralHead-FF | MarioNETte | MarioNETte+LT |

Figure 11: Qualitative results of one-shot self-reenactment setting on VoxCeleb1.

| Target | Driver | X2Face | NeuralHead-FF | MarioNETte | MarioNETte+LT |

Figure 12: Qualitative results of few-shot self-reenactment setting on VoxCeleb1.

| Target | Driver | X2Face | Monkey-Net | NeuralHead-FF | MarioNETte | MarioNETte+LT |

Figure 13: Qualitative results of one-shot reenactment under different identity setting on VoxCeleb1.

| Target | Driver | X2Face | NeuralHead-FF | MarioNETte | MarioNETte+LT |

Figure 14: Qualitative results of few-shot reenactment under different identity setting on VoxCeleb1.

| Target | Driver | X2Face | Monkey-Net | NeuralHead-FF | MarioNETte | MarioNETte+LT |

Figure 15: Qualitative results of one-shot self-reenactment setting on CelebV.

| Target | Driver | X2Face | NeuralHead-FF | MarioNETte | MarioNETte+LT |

Figure 16: Qualitative results of few-shot self-reenactment setting on CelebV.

| Target | Driver | X2Face | NeuralHead-FF | MarioNETte | MarioNETte+LT |

Figure 17: Qualitative results of few-shot reenactment under different identity setting on CelebV.
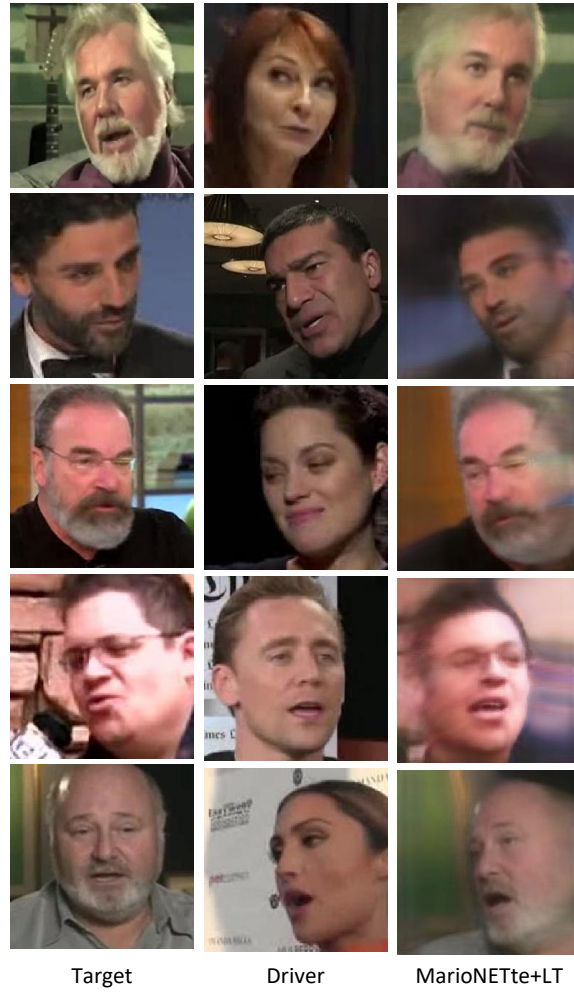
Target   Driver   MarioNETte+LT

Figure 18: Failure cases generated by MarioNETte+LT while performing one-shot reenactment under different identity setting on VoxCeleb1.